

---

# Unifying Voxel-based Representation with Transformer for 3D Object Detection

---

**Yanwei Li<sup>1</sup> Yilun Chen<sup>1</sup> Xiaojuan Qi<sup>2</sup> Zeming Li<sup>3</sup> Jian Sun<sup>3</sup> Jiaya Jia<sup>1,4</sup>**

The Chinese University of Hong Kong<sup>1</sup> The University of Hong Kong<sup>2</sup>  
MEGVII Technology<sup>3</sup> SmartMore<sup>4</sup>

## Abstract

In this work, we present a unified framework for multi-modality 3D object detection, named UVTR. The proposed method aims to unify multi-modality representations in the voxel space for accurate and robust single- or cross-modality 3D detection. To this end, the modality-specific space is first designed to represent different inputs in the voxel feature space. Different from previous work, our approach preserves the voxel space without height compression to alleviate semantic ambiguity and enable spatial interactions. Benefit from the unified manner, cross-modality interaction is then proposed to make full use of inherent properties from different sensors, including knowledge transfer and modality fusion. In this way, geometry-aware expressions in point clouds and context-rich features in images are well utilized for better performance and robustness. The transformer decoder is applied to efficiently sample features from the unified space with learnable positions, which facilitates object-level interactions. In general, UVTR presents an early attempt to represent different modalities in a unified framework. It surpasses previous work in single- and multi-modality entries and achieves leading performance in the nuScenes *test* set with 69.7%, 55.1%, and 71.1% NDS for LiDAR, camera, and multi-modality inputs, respectively. Code is made available at <https://github.com/dvlab-research/UVTR>.

## 1 Introduction

Detecting 3D objects with multi-modality sensors (*i.e.*, LiDAR and camera) is regarded as a fundamental task in real-world scenes. For accurate object detection, data from different modalities are utilized to provide complementary knowledge, like accurate positions from point clouds and rich context from images. Toward this purpose, a unified representation is essential to facilitate knowledge transfer and feature fusion across modalities. However, due to the lack of accurate depth from cameras, images can not be naturally represented in voxel space like that of point clouds.

In the unified progress, several representations have been studied that can be roughly separated into input- and feature-level streams. For the first one, multi-modality data is aligned at the beginning of network. In particular, pseudo point clouds in Figure 1a are transformed from image aided by predicted depth [1, 2], while the range-view image in Figure 1b is projected from point clouds [3, 4]. Because of inaccurate depth in pseudo point clouds and collapsed 3D geometry in range-view images, the spatial structure of data is damaged, which brings inferior results. For feature-level method, a typical approach is to transform image features as frustum and then compress to BEV space [5, 6], like that in Figure 1c. However, due to ray-like trajectories in the frustum [7], height compression at each position aggregates features from various objects and thus introduces semantic ambiguity. Meanwhile, other implicit manners in contemporary work [8, 9, 10] can hardly support explicit feature interactions in 3D space and restrict further knowledge transfer. Therefore, a more unified representation is desired to bridge modality gap and facilitate interactions from multiple aspects.

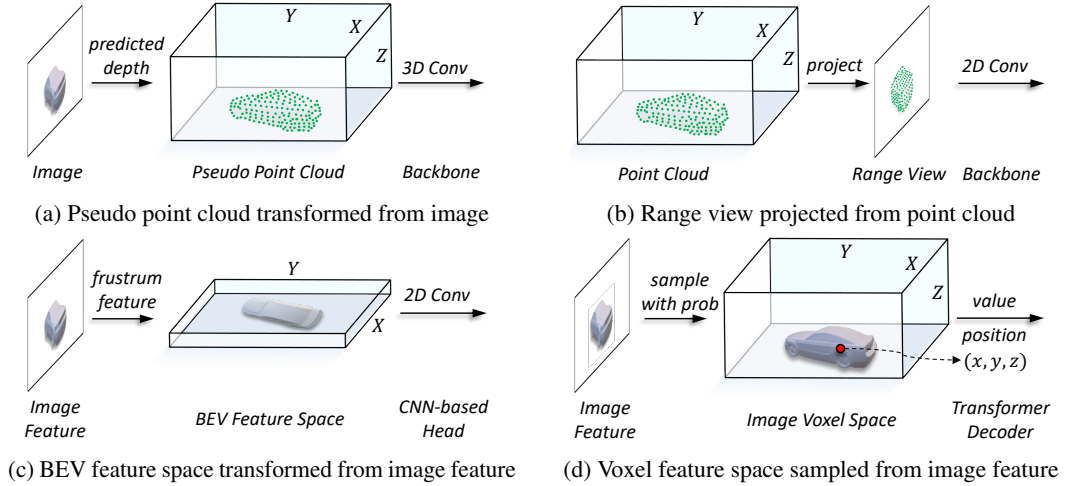


Figure 1: Toy example of methods for unified representation. Compared with others, the proposed manner in 1d constructs the voxel space by sampling features from the image plane and represents multi-modalities uniformly *without* height-level compression in 1c that brings semantic ambiguity.

In this paper, we present a simple yet effective framework to unify the voxel-based representation with transformer, called UVTR. In particular, features from images and point clouds are represented and interacted in the explicit voxel-based space. For images, we construct the voxel space by sampling features from the image plane according to predicted depth scores and geometric constraints, as briefly depicted in Figure 1d. For point clouds, the accurate position naturally allows us to associate features to voxels. Then, voxel encoder is introduced for spatial interaction that establishes the relationship among adjacent features. In this way, cross-modality interaction is naturally conducted with features in each voxel space. For object-level interaction, deformable transformer [11] is adopted as the decoder that samples specific feature for each object query with position  $(x, y, z)$  in the unified voxel space, as illustrated in Figure 1d. Meanwhile, the introduction of 3D query position efficiently alleviates the semantic ambiguity brought by height compression in BEV space as analysed before.

Compared with previous and even concurrent studies [8, 9], more key advances can be achieved with the proposed framework. *First*, the explicit voxel-based representation supports spatial interaction in 3D space and multi-frame scenes that bring significant improvements. *Second*, the proposed unified manner facilitates cross-modality learning and can be naturally applied for knowledge transfer and feature fusion, which further boosts the performance. *Finally*, data augmentation for both modalities can be directly synchronized in the voxel space without the complex aligning process [12, 7].

The overall framework, called UVTR, can be easily instantiated and improved with various image- or voxel-based backbones for single- and multi-modality 3D object detection. Extensive empirical studies are conducted in Section 4 to reveal the effect of each component. The proposed UVTR attains leading performance with robustness on various settings. For single-modality input, it achieves **69.7%** NDS with point clouds and 52.2% NDS with images on nuScenes *test* set. If given multi-frame images, the camera-based manner can be further improved to **55.1%** NDS. For multi-modality input, UVTR reaches **71.1%** NDS with simple fine-tuning based on pretrained models for each modality.

## 2 Related Work

**LiDAR-based 3D Detection.** With point clouds captured from LiDAR, traditional methods process the irregular input and generate 3D boxes with different representations, *e.g.*, point, voxel, and range view. Point-based detectors usually aggregate features from raw point clouds with set abstraction [13] and then predict box proposals [14, 15, 16]. For voxel-based methods, point clouds are transformed into regular grids and processed with 3D sparse convolutions [17, 18] or 2D convolutions [19, 20, 21] directly. Final predictions are usually generated on top of the bird-eye view (BEV) space with the flattened height axis [22, 23, 24]. There are also studies [3, 4] that project point clouds to range view and process them like images. However, due to the collapsed 3D geometry in range-view images,

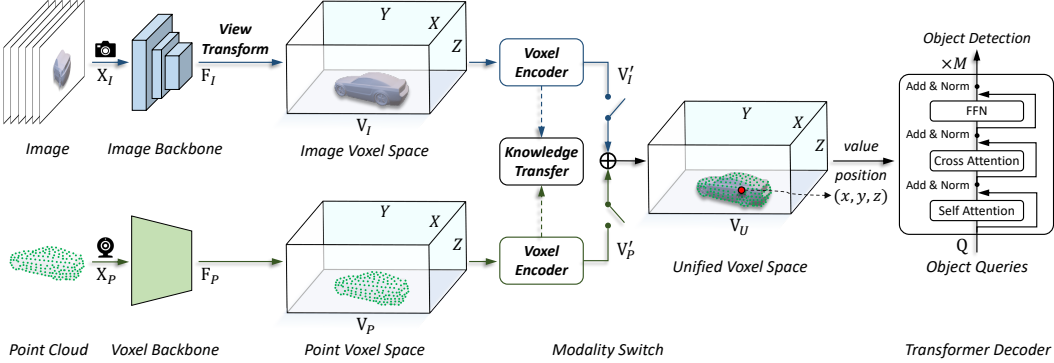


Figure 2: The framework of UVTR with multi-modality input. Given single- or multi-frame images and point clouds, we first process them in individual backbone and convert to modality-specific space  $\mathbf{V}_I$  and  $\mathbf{V}_P$ , where view transform is utilized for that of image. In voxel encoder, features are spatially interacted, and knowledge transfer is easily supported during training. Single- or multi-modality features are selected via modality switch according to different settings. Finally, transformer decoder is utilized for prediction by sampling features from the unified space  $\mathbf{V}_U$  with learnable positions.

the relationship in point clouds cannot be fully explored. In this work, we follow the voxel-based pipeline but keep the fine-grained voxel space without height compression, as shown in Figure 2.

**Camera-based 3D Detection.** Camera-based methods perform 3D detection on single- or multi-view images. With monocular image, previous approaches try to predict 3D boxes based on image features directly [25, 26, 27] or utilize the middle representation [1, 2, 5]. For multi-view input, image features are usually optimized in the constructed 3D geometry volume [28, 29]. Most recently, multi-view features are projected and merged in the frustum feature space with the aid of predicted depth [6]. Following the LiDAR-based paradigm, the frustum feature is collapsed to the BEV space, as briefly introduced in Figure 1c. However, the accuracy of the predicted depth map is much inferior to that of LiDAR, which brings semantic ambiguity to BEV space. Other recent studies try to capture geometry clues from multi-view images in an implicit manner [8, 10], which losses the chance for direct spatial interactions. In this paper, we represent image features in an explicit voxel space to alleviate the semantic ambiguity and facilitate further feature interactions, as depicted in Figure 1d.

**Cross-modality Interaction.** With input data from various sensors, cross-modality interaction is conducted to benefit from different inputs, *e.g.*, modality fusion and knowledge transfer. For modality fusion, the model takes data from different sensors and conducts fusion at point- and instance-level. Specifically, point-level fusion [30, 31, 32, 7] combines features from different modalities at the early stage of the network, which enables sufficient interaction. And instance-level fusion [33, 34, 35] is usually applied at the later stage to combine object-level features. Cross-modality knowledge transfer aims to distill specific knowledge [36] across modalities in the training phase. Compared with cross-modality fusion, knowledge transfer is seldom studied for 3D object detection. A prior work is LIGA-Stereo [37] that transfers geometry-aware representations from LiDAR to stereo images via distillation. Different from [37], UVTR represents each modality in a unified manner and supports cross-modality fusion and knowledge transfer simultaneously, which further enables distillation from multi-modality or consecutive frames to the single input.

### 3 UVTR Framework

The overall framework of UVTR is relatively simple: modality-specific space is constructed to unify the representation of inputs; cross-modality interaction is designed for feature learning across spaces; and transformer decoder is introduced for object-level interaction and final prediction.

#### 3.1 Modality-specific Space

Given images  $\mathbf{X}_I$  captured from cameras and point cloud  $\mathbf{X}_P$  from LiDAR, different branches are utilized to respectively generate and enhance voxel space for each modality, as presented in Figure 2.

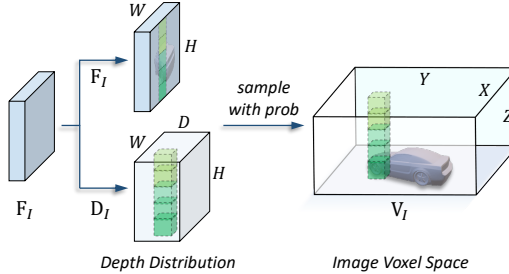


Figure 3: Details in the view transform.

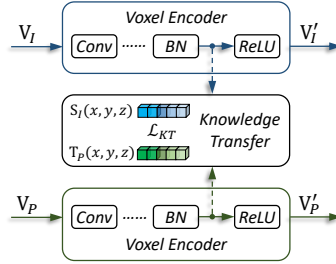


Figure 4: Details in the knowledge transfer.

**Image Voxel Space.** For image voxel space, a shared backbone is adopted to extract features from multi-view or multi-frame images. In this process, FPN [38] is utilized for multi-scale context aggregation that is summed to formulate the feature  $\mathbf{F}_I \in \mathbb{R}^{H \times W \times C}$ , where  $H$  and  $W$  vary with FPN stages. To construct the voxel feature for images, we then transform the image feature of each view to the predefined space with the designed view transform in Figure 3. Motivated by [39, 5], we first generate the depth distribution  $\mathbf{D}_I \in \mathbb{R}^{D \times H \times W}$  of each image with a single convolution as

$$\mathbf{D}_I(u, v) = \text{Softmax}(\text{Conv}(\mathbf{F}_I)(u, v)). \quad (1)$$

Here,  $(u, v)$  indicates coordinate in the image plane, and  $D$  is set to 64 by default. With the predicted  $\mathbf{D}_I$  in  $D$  depth bins, we can easily get the depth distribution of corresponding pixel in  $\mathbf{F}_I$ . Let  $(x, y, z)$  indicates a sampling point that is generated at the center of each bin from the voxel space  $\mathbf{V}_I$ . The sampling point  $(u, v, d)$  in the image plane is calculated from  $(x, y, z)$  with the calibration matrix  $\mathbf{P}$ , where  $d$  denotes the reference depth along axis  $D$  of  $\mathbf{D}_I$ . Thus, the corresponding feature in voxel space  $\mathbf{V}_I$  is easily captured by

$$\mathbf{V}_I(x, y, z) = \mathbf{D}_I(u, v, d) \times \mathbf{F}_I(u, v), \quad (2)$$

where  $\mathbf{D}_I(u, v, d)$  represents the occupancy probability of feature  $\mathbf{F}_I(u, v)$  in voxel  $(x, y, z)$ . For the multi-frame setting with  $n$  sweeps, we use the shared network for all of them and formulate  $n$  voxel spaces in total. In this process, each calibration matrix  $\mathbf{P}$  is aligned to the ego vehicle in the initial frame. To gather temporal cues in each voxel space, relative time offsets from the initial frame are attached along the channel axis and merged using a single convolution. Then,  $n$  voxel spaces are concatenated together, and the space-level fusion is conducted with a convolutional layer. In this way, features along the temporal dimension are integrated into a unified space  $\mathbf{V}_I$ , which is proved to bring significant gain in Table 3. Different from methods [5, 6] for BEV space, we preserve the 3D voxel space without collapsing in  $Z$  axis to avoid the aforementioned semantic ambiguity and enable further interactions. The effectiveness of the 3D voxel space is empirically studied in Table 1.

**Point Voxel Space.** With the accurate position, we naturally split point cloud  $\mathbf{X}_P$  into several regular voxels. Then, the voxel backbone in Figure 2 is utilized to process input voxels with sparse convolution [17]. To enhance multi-scale features in the generated voxel space, parallel heads with various strides are designed to extract feature  $\mathbf{F}_P$  from the output. In particular, several 2D convolutions are applied in each head to aggregate the spatial cues at each height. Then, multi-scale features are upsampled to a same resolution and summed together to formulate the voxel space  $\mathbf{V}_P \in \mathbb{R}^{X \times Y \times Z \times C}$ . For multi-frame setting with  $n$  sweeps, we follow previous work [24] and attach all point clouds together with relative time offsets to formulate the input  $\mathbf{X}_P$ .

Due to the accurate position of point cloud, the semantic ambiguity in  $Z$  axis is much reduced compared with that of images. But we still preserve the 3D space  $\mathbf{V}_P$  without height compression for convenient cross-modality interaction in Section 3.2 and fine-grained object interaction in Section 3.3. This is also proved to bring superior experimental result in Table 1.

**Voxel Encoder.** In the above-generated space  $\mathbf{V}_I$ , features of adjacent voxels projected from different views have no connection with each other. To solve this issue and facilitate local feature interaction, the voxel encoder is proposed in each voxel space, as presented in Figure 2. Specifically, we keep the simplicity of UVTR, and only three basic convolutional blocks are applied in each voxel encoder of Figure 4. In this process, features in each space  $\mathbf{V}_I$  or  $\mathbf{V}_P$  are aggregated in both coplanar and vertical dimensions. The spatial interaction in voxel space establishes connections among adjacent features, which is proved to be essential in Table 2, especially for  $\mathbf{V}_I$ .

### 3.2 Cross-modality Interaction

With the unified representation in space  $\mathbf{V}_I$  and  $\mathbf{V}_P$ , interactions across modalities can be easily conducted. Given the prior that LiDAR is advanced in localization and cameras provide context for classification, the cross-modality interaction is proposed from two folds, *i.e.*, transferring geometry-aware knowledge to images and fusing context-aware features with point clouds.

**Knowledge Transfer.** Considering single modality input in the inference stage, knowledge transfer is first designed to optimize features of the student with guidance from the teacher during training. Due to inherent properties, the geometry structure contained in images can be further exploited with the aid of point clouds, while the rich context in images can hardly be transferred to sparse point clouds. Therefore, we mainly focus on transferring knowledge from the geometry-rich modality to the poor one in this work. Benefit from unified feature spaces, the cross-modality transfer can be easily supported, as illustrated in Figure 4. In particular, we take features before the last ReLU layer in the voxel encoder of  $\mathbf{V}_P$  as the geometry-rich teacher, marked as  $\mathbf{T}_P$ . Meanwhile, the feature in the same position of  $\mathbf{V}_I$  is taken as the geometry-poor student, denoted as  $\mathbf{S}_I$ . If we take one object query position  $(x, y, z)$  from Section 3.3, the feature distance for knowledge transfer is formulated as

$$d_{KT} = PL_2(\mathbf{T}_P(x, y, z), \mathbf{S}_I(x, y, z)), \quad (3)$$

where  $PL_2$  represents the partial  $L_2$  distance [40]. Without bells-and-whistles, the optimization objective for knowledge transfer is averaged from  $N$  object queries of transformer decoder in Section 3.3, namely  $\mathcal{L}_{KT} = \frac{1}{N} \sum_i (d_{KT})$ . Given the object position in each query, we can directly minimize the object-level distance with no need to exclude background features like [37]. In a similar pipeline, the knowledge transfer is further extended to support more input streams, like multi-frame images and multi-modality data. The proposed cross-modality knowledge transfer is flexible with input modalities and brings consistent gains over various baselines in Tables 5 and 7.

**Modality Fusion.** Different from the knowledge transfer, modality fusion aims to better utilize all modalities in both training and inference stages. Thanks to the unified representation of each modality, feature fusion can be naturally applied. To be specific, given the processed feature space  $\mathbf{V}'_I$  and  $\mathbf{V}'_P$ , we first select candidate modality for final prediction via modality switch, as depicted in Figure 2. That means we support single- or multi-modality input for prediction according to different settings. If both modalities are taken,  $\mathbf{V}'_I$  and  $\mathbf{V}'_P$  are added together to formulate the unified voxel space  $\mathbf{V}_U \in \mathbb{R}^{X \times Y \times Z \times C}$ . In this way, both modalities are well expressed in a unified manner, which can be further fused with a single convolution. The voxel space  $\mathbf{V}_U$  unifies modalities with the explicit representation, which provides an expressive value space for object interactions in Section 3.3.

### 3.3 Transformer Decoder

To obtain accurate and robust predictions, the transformer decoder is utilized for further object-level interaction in the unified voxel space  $\mathbf{V}_U$ . We draw inspirations from deformable DETR [11] and apply reference positions to efficiently sample representative features. In particular, we first initialize  $N$  object queries  $\mathbf{Q} \in \mathbb{R}^{N \times C}$  and generate  $N$  reference points from object query embedding. Then, object queries are interacted with each other in the self-attention module and summed via skip-connection, as shown in Figure 2. Let  $q$  represents a specific query in  $\mathbf{Q}$  with corresponding reference point  $p = (x, y, z)$ . The process of the cross-attention module in Figure 2 is modeled as

$$\text{CrossAttn}(q, \mathbf{V}_U(p)) = \text{DeformAttn}(q, p, \mathbf{V}_U), \quad (4)$$

where  $\mathbf{V}_U(p)$  denotes the sampled feature at  $(x, y, z)$  of  $\mathbf{V}_U$ , and DeformAttn indicates the deformable attention in [11]. With the feed-forward network and normalization, each object query can easily interact with unified features from  $\mathbf{V}_U$  inside each block. There are total  $M$  blocks in the transformer decoder, where  $M$  is respectively set to 3 and 6 for LiDAR-based and camera-based settings. Finally, a shared MLP head is utilized for prediction according to the output of each block. And iterative box refinement [11, 8] is applied to refine 3D bounding boxes based on the predictions.

### 3.4 Optimization Objectives

Following a general paradigm in recent transformers [41, 11], Hungarian algorithm [42] is adopted for one-to-one target assignment in the training phase. Thus, a set-to-set loss  $\mathcal{L}_{Det}$  is computed to optimize detection results, including box regression loss and classification loss. If knowledge transfer is applied, the loss  $\mathcal{L}_{KT}$  is contained to reduce cross-modality feature distance with a weight 0.01.

## 4 Experiments

In this section, we first introduce our detailed experimental setup. Then, analyses of each component are conducted on different modalities. Comparisons with several leading benchmarks on the nuScenes [43] dataset are presented in the end. More results are attached in *supplementary material*.

### 4.1 Experimental Setup

**Dataset.** nuScenes [43] dataset is a large-scale benchmark for autonomous driving, which is widely adopted for single- or multi-modality 3D object detection. It contains 700, 150, 150 scenes in the *train*, *val*, and *test* set, respectively. We use the synced data with 10 object categories that are captured from a 32-beam LiDAR at 20Hz and six cameras in a 360-degree field of view at 12Hz. Only annotations of keyframes are given at 2Hz. Here, ablation studies are optimized on a mini 1/4 *train* split by default, and final models are optimized on the whole *train* set.

**Implementation Details.** In this work, we conduct experiments on different modalities with 900 object queries  $\mathbf{Q}$ . Constructed voxel spaces  $\mathbf{V}_I$ ,  $\mathbf{V}_P$ , and  $\mathbf{V}_U$  share the same shape  $128 \times 128 \times Z$ , where  $Z$  indicates the height of voxel space and is further investigated in Table 1. The channel number  $C$  in voxel spaces and transformer decoder is set to 256. And the amount of block  $M$  in the decoder is set to 3, 6, and 6 for LiDAR-based, camera-based, and fusion settings, respectively. In particular, for the LiDAR-based setting, only the branch with voxel space  $\mathbf{V}_P$  is kept. With grid size  $0.1m$ , the input point clouds are filtered in range  $[-51.2m, 51.2m]$  for  $X$  and  $Y$  axis with  $[-5.0m, 3.0m]$  for  $Z$  axis. While for grid size  $0.075m$ , the range in  $X$  and  $Y$  axis is modified to  $[-54.0m, 54.0m]$ . The framework is trained with AdamW optimizer with an initial learning rate  $2e^{-5}$  for 20 epochs. For a camera-based setting, the network is optimized with an initial learning rate  $1e^{-4}$  for 24 epochs. As for fusion setting, we initialize two modality-specific branches with corresponding pretrained models and optimize the whole framework with an initial learning rate  $4e^{-5}$  for 20 epochs. For more details about network and optimization, please refer to *supplementary material*.

### 4.2 Component-wise Analysis

Due to the large dataset scale, we use a 1/4 split of the nuScenes *train* set for efficient validation process in *this subsection*. The data in the mini-split is randomly sampled from the original *train* set.

**Effect of Height in Voxel Space.** As elaborated in Section 3.1, the height axis  $Z$  plays a vital role in voxel space, especially for camera-based  $\mathbf{V}_I$ . In Table 1, we validate this with different heights on both modalities. Compared with the BEV space with height 1, the increase in height contributes significantly for camera-based  $\mathbf{V}_I$ , which respectively improves 3.1% and 4.2% NDS with height 5 and 11. Consistent with our analysis, the gain brought by increase of height contributes less to that of LiDAR because of the accurate position, which is up to 1% NDS and 1.9% mAP.

**Operations in Voxel Encoder.** The voxel encoder in Section 3.1 aims to facilitate spatial feature interactions that are essential, especially in the camera-based manner. As presented in Table 2, camera-based network cannot converge if given no spatial interaction. For LiDAR-based network, it performs satisfactorily without the voxel encoder, which can be attributed to the established relations at the early stage. Overall, for both of them, 3D spatial interaction still plays a vital role and improves 2.6% and 0.6% NDS over 2D convolution for the camera- and LiDAR-based methods, respectively. It further proves the importance of interaction in height  $Z$  as analyzed above.

Table 1: Comparisons among different heights  $Z$  in voxel space on nuScenes *val* set.

modality	height	NDS(%)	mAP(%)
Camera	1	31.4	24.9
	5	34.5	27.0
	11	<b>35.6</b>	<b>28.7</b>
LiDAR	1	62.8	54.4
	5	63.8	55.5
	11	<b>63.8</b>	<b>56.3</b>

Table 2: Comparisons among different operations in voxel encoder on nuScenes *val* set.

modality	type	NDS(%)	mAP(%)
Camera	None	12.0	2.5
	Conv2D	31.9	24.8
	Conv3D	<b>34.5</b>	<b>27.0</b>
LiDAR	None	63.1	54.3
	Conv2D	63.2	54.6
	Conv3D	<b>63.8</b>	<b>55.5</b>

Table 3: Comparisons among different number of frames on nuScenes *val* set. *sweep* denotes the sweep number of multi-frame input.

<i>modality</i>	<i>sweep</i>	NDS(%)	mAP(%)
Camera	1	34.5	27.0
	3	38.0	28.7
	5	<b>39.5</b>	<b>29.4</b>
LiDAR	1	45.7	42.8
	10	<b>63.8</b>	<b>55.5</b>

Table 5: Comparisons among different knowledge transfer settings on nuScenes *val* set. CS denotes multi-frame camera sweeps.

<i>student</i>	<i>teacher</i>	NDS(%)	mAP(%)
Camera	–	34.5	27.0
	CS	36.3	28.1
	LiDAR	36.4	28.2
	Multi-mod	<b>37.1</b>	<b>28.8</b>
LiDAR	–	63.8	55.5
	Multi-mod	<b>64.4</b>	<b>56.1</b>

Table 4: Comparisons among different models for voxel space construction on nuScenes *val* set. H and V denote space height and grid size.

<i>modality</i>	<i>voxel net</i>	NDS(%)	mAP(%)
Camera	R50-H5	34.5	27.0
	R50-H11	35.6	28.7
	R101-H11	<b>39.4</b>	<b>32.0</b>
LiDAR	V0.1	63.8	55.5
	V0.075	<b>64.3</b>	<b>56.3</b>

Table 6: Comparisons among different network settings for cross-modality fusion on nuScenes *val* set. V denotes the split voxel grid size.

<i>camera</i>	<i>lidar</i>	NDS(%)	mAP(%)
R50	–	34.5	27.0
–	V0.1	63.8	55.5
R50	V0.1	65.1	59.0
	V0.075	<b>65.6</b>	<b>60.1</b>
R101	V0.1	65.4	59.4
	V0.075	<b>66.3</b>	<b>61.0</b>

**Effect of Multi-frame Input.** To further release the potential of the designed paradigm, we input multi-frame sweeps and represent them in each voxel space, as shown in Table 3. With more input frames, networks for both modalities achieve consistent gains. The performance gap reaches 5% and 18.1% NDS for the camera- and LiDAR-based manner with 5 and 10 sweeps, respectively.

**Networks for Voxel Space.** In Table 4, we exploit the network for voxel space generation. It is clear that the deeper network with larger voxel space contributes more to the final result. With ResNet-101 and height 11 for space  $V_I$ , the camera-based method attains nearly 5% gains over the baseline in both NDS and mAP. For LiDAR-based manner, the model performs slightly better with finer grid size that brings higher resolution to voxel space. It means the image-based voxel space requires strong backbones to extract expressive features, while the LiDAR-based one is less dependent on that.

**Knowledge Transfer.** Benefit from the unified representation, knowledge can be easily transferred across modalities. In Table 5, we compare combinations with different students and teachers. In particular, the camera-based student captures geometry-aware cues from camera sweeps or the LiDAR-based teacher, which brings up to 1.9% NDS gain. If coupled with context features in the multi-modality setting, the gap is enlarged to 2.6% NDS and 1.8% mAP. For the LiDAR-based student, the increase brought by knowledge transfer saturated with 0.6% NDS. This can be attributed to that rich context in images can not be well expressed only with sparse points during inference. Therefore, images are required as input if rich context is supplemented, like the following fusion part.

**Cross-modality Fusion.** In Table 6, we validate capability of UVTR with cross-modality fusion. As presented in the table, feature fusion brings significant gains over the single modality. And the LiDAR-based representation dominates the final results, while the camera-based one provides supplementary context. It is reasonable because point clouds are more accurate in position and more representative in geometry expression. Cameras still provide sufficient context for better classification, which yields up to 1.6% NDS and 3.9% mAP gain compared with the LiDAR-based baseline. With finer voxel grids, the performance gap is enlarged to 2.5% NDS and 5.5% mAP.

### 4.3 Main Results

In this section, we first report results with various modalities that are optimized on the whole *train* set. Then, we give analyses of the framework robustness, including camera view drop and translational noise. Comparisons with leading methods on the nuScenes *test* set are presented in the end.

Table 7: Comparisons among different methods with a single model on the nuScenes *val* set. We compare with classic methods on different modalities *without* test-time augmentation.  $\dagger$  denotes the implementation from MMDetection3D [44]. L, C, CS, and M indicate the LiDAR, Camera, Camera Sweep, and Multi-modality input, respectively. L2 represents knowledge transfer from LiDAR.

Method	Backbone	NDS(%)	mAP(%)	mATE $\downarrow$	mASE $\downarrow$	mAOE $\downarrow$	mAVE $\downarrow$	mAAE $\downarrow$
<i>LiDAR-based</i>								
CenterPoint $\dagger$ [24]	V0.1	64.9	56.6	0.291	0.252	0.324	0.284	0.189
UVTR-L	V0.1	66.4	59.3	0.345	0.259	0.313	0.218	0.185
UVTR-L	V0.075	<b>67.7</b>	<b>60.9</b>	0.334	0.257	0.300	0.204	0.182
<i>Camera-based</i>								
DETR3D [8]	R101	42.5	34.6	0.773	0.268	0.383	0.842	0.216
UVTR-C	R50	41.9	33.3	0.793	0.276	0.454	0.760	0.196
UVTR-C	R101	44.1	36.2	0.758	0.272	0.410	0.758	0.203
UVTR-CS	R50	47.2	36.2	0.756	0.276	0.399	0.467	0.189
UVTR-CS	R101	48.3	37.9	0.731	0.267	0.350	0.510	0.200
UVTR-L2C	R101	45.0	37.2	0.735	0.269	0.397	0.761	0.193
UVTR-L2CS	R101	<b>48.8</b>	<b>39.2</b>	0.720	0.268	0.354	0.534	0.206
<i>LiDAR+Camera</i>								
FUTR3D [9]	V0.075-R101	68.3	64.5	-	-	-	-	-
UVTR-M	V0.075-R101	<b>70.2</b>	<b>65.4</b>	0.332	0.258	0.268	0.212	0.177

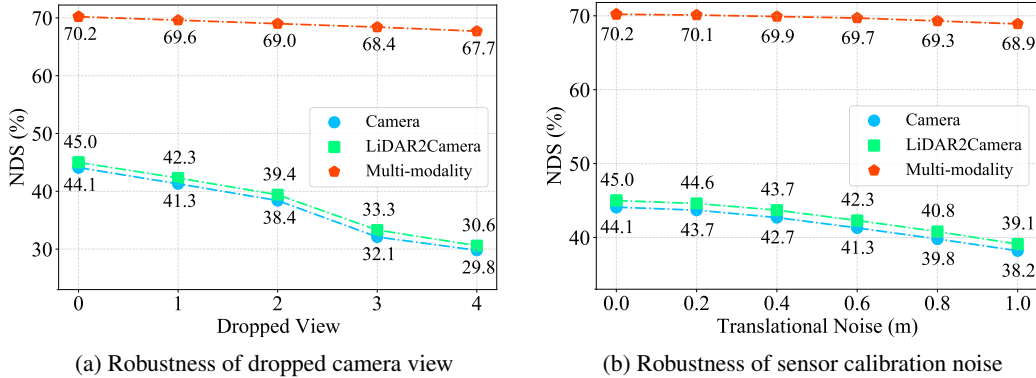


Figure 5: We validate the robustness of UVTR by adding two typical errors during inference. For dropped view in 5a, we randomly drop a fix number of camera views to simulate the camera failure. For sensor noise in 5b, we randomly add translational noises in LiDAR to camera calibration matrix.

**Results with Different Modalities.** In Table 7, we carry out experiments with different modalities on the nuScenes *val* set. Compared with classic methods, UVTR achieves significant improvement. In particular, for LiDAR-based method, it attains 1.5% NDS and 2.7% mAP gain over CenterPoint [24]. And a finer resolution contributes better results with 67.7% NDS. For camera-based manner, UVTR-C performs better in single frame setting with 1.6% NDS gain over DETR3D [8]. If applied knowledge transfer in UVTR-L2C, the gap is enlarged to 2.5% NDS. The performance improves with more frames and attains up to 48.8% NDS. For multi-modality input, UVTR-M achieves 4.5% mAP gain over UVTR-L and outperforms the contemporary FUTR3D [9] with 1.9% NDS in a same setting.

**Robustness of the Framework.** To validate the robustness of UVTR, we simulate two typical sensor errors during inference in Figure 5. For loss of view, the multi-modality manner achieves well robustness in Figure 5a. Because LiDAR can still capture surrounding scenes if cameras are offline. As for the camera-based manner, the model losses inputs from dropped scenes, but the network still works well and outputs predictions within the field of view. For sensor jitter in Figure 5b, the model performs stable especially in the multi-modality setting because of the accurate perception from LiDAR. Meanwhile, knowledge transfer consistently improves performance in both settings.

Table 8: Comparisons among leading methods with a single model on the nuScenes *test* set. L, C, CS, and M indicate the LiDAR, Camera, Camera Sweep, and Multi-modality input, respectively. L2 represents knowledge transfer from LiDAR. Flipping augmentation is adopted for LiDAR. It should be noted that the performance of UVTR-L2CS3 can be further improved with more than 3 sweeps.

Method	Backbone	NDS(%)	mAP(%)	mATE $\downarrow$	mASE $\downarrow$	mAOE $\downarrow$	mAVE $\downarrow$	mAAE $\downarrow$
<i>LiDAR-based</i>								
3DSSD [45]	Point-based	56.4	42.6	-	-	-	-	-
CenterPoint [24]	V0.075	65.5	58.0	-	-	-	-	-
HotSpotNet [46]	V0.1	66.0	59.3	0.274	0.239	0.384	0.333	0.133
AFDetV2 [47]	V0.075	68.5	62.4	0.257	0.234	0.341	0.299	0.137
UVTR-L	V0.075	<b>69.7</b>	<b>63.9</b>	0.302	0.246	0.350	0.207	0.123
<i>Camera-based</i>								
FCOS3D [27]	R101	42.8	35.8	0.690	0.249	0.452	1.434	0.124
DD3D [48]	V2-99	47.7	41.8	0.572	0.249	0.368	1.014	0.124
DETR3D [8]	V2-99	47.9	41.2	0.641	0.255	0.394	0.845	0.133
BEVDet [6]	V2-99	48.8	42.4	0.524	0.242	0.373	0.950	0.148
PETR [10]	V2-99	50.4	44.1	0.593	0.249	0.383	0.808	0.132
UVTR-L2C	V2-99	52.2	45.2	0.612	0.256	0.385	0.664	0.125
UVTR-L2CS3	V2-99	<b>55.1</b>	<b>47.2</b>	0.577	0.253	0.391	0.508	0.123
<i>LiDAR+Camera</i>								
FusionPainting [49]	V0.075-R50	70.4	66.3	-	-	-	-	-
MVP [32]	V0.075-DLA34	70.5	66.4	-	-	-	-	-
PointAugmenting [50]	V0.075-DLA34	71.0	66.8	-	-	-	-	-
UVTR-M	V0.075-R101	<b>71.1</b>	<b>67.1</b>	0.306	0.245	0.351	0.225	0.124

**Comparison with Leading Methods.** In Table 8, we present comparisons with leading methods on the nuScenes *test* set. For LiDAR-based method, UVTR-L surpasses AFDetV2 [47] with 1.2% NDS and attains 69.7% NDS. For camera-based manner, with single frame, UVTR-L2C outperforms PETR [10] with 1.8% NDS and 1.1% mAP. With 3 camera sweeps, UVTR-L2CS3 obtains significant gain and attains 55.1% NDS, which can be further improved with more frames. For the multi-modality setting, we directly adopt pretrained models from LiDAR- and camera-based manner with simple fine-tuning without bells-and-whistles. Compared with similar approaches without special module, UVTR-M achieves 71.1% NDS and 67.1% mAP, which is on par with leading approaches.

## 5 Discussion and Conclusion

We presented the UVTR, a conceptually simple yet effective framework for multi-modality 3D object detection. The key innovation lies in that it unifies the voxel-based representation for different modalities and facilitates multi-level interactions. In particular, it uniformly encodes inputs from different sensors in the modality-specific space to reduce the semantic ambiguity and enable spatial interaction. With the unified representation, the cross-modality interaction can be easily conducted for knowledge transfer and modality fusion. Moreover, object-level interactions in the unified space are further supported by the transformer decoder for accurate and robust detection. Experiments on the nuScenes dataset prove the effectiveness of UVTR, which attains consistent improvements over various benchmarks and surpasses previous methods with leading performance.

There still exist certain limitations in the current method. First, to construct voxel space for multi-view images, we need to process all of them in the shared image backbone, which brings computational cost, especially for multi-frame setting. Moreover, we construct the voxel space with a spatial resolution  $128 \times 128$ . We believe a higher resolution and more image frames could bring stronger voxel space with better results, which remains to be explored.

**Societal Impacts.** The proposed method focuses on 3D object detection that can be used in autonomous driving. Theoretically, a better 3D detector leads to safer autonomous vehicles. However, in the short term, the current technique could not solve all the corner cases and extreme situations. It may bring potential risk to the decision process in real-world autonomous systems.

## References

- [1] Yan Wang, Wei-Lun Chao, Divyansh Garg, Bharath Hariharan, Mark Campbell, and Kilian Q Weinberger. Pseudo-lidar from visual depth estimation: Bridging the gap in 3d object detection for autonomous driving. In *IEEE Conference on Computer Vision and Pattern Recognition*, 2019.
- [2] Yurong You, Yan Wang, Wei-Lun Chao, Divyansh Garg, Geoff Pleiss, Bharath Hariharan, Mark Campbell, and Kilian Q Weinberger. Pseudo-lidar++: Accurate depth for 3d object detection in autonomous driving. In *International Conference on Learning Representations*, 2020.
- [3] Bo Li, Tianlei Zhang, and Tian Xia. Vehicle detection from 3d lidar using fully convolutional network. *arXiv:1608.07916*, 2016.
- [4] Lue Fan, Xuan Xiong, Feng Wang, Naiyan Wang, and Zhaoxiang Zhang. Rangedet: In defense of range view for lidar-based 3d object detection. In *IEEE/CVF International Conference on Computer Vision*, 2021.
- [5] Cody Reading, Ali Harakeh, Julia Chae, and Steven L Waslander. Categorical depth distribution network for monocular 3d object detection. In *IEEE Conference on Computer Vision and Pattern Recognition*, 2021.
- [6] Junjie Huang, Guan Huang, Zheng Zhu, and Dalong Du. Bevdet: High-performance multi-camera 3d object detection in bird-eye-view. *arXiv:2112.11790*, 2021.
- [7] Yanwei Li, Xiaojuan Qi, Yukang Chen, Liwei Wang, Zeming Li, Jian Sun, and Jiaya Jia. Voxel field fusion for 3d object detection. In *IEEE Conference on Computer Vision and Pattern Recognition*, 2022.
- [8] Yue Wang, Vitor Campagnolo Guizilini, Tianyuan Zhang, Yilun Wang, Hang Zhao, and Justin Solomon. Detr3d: 3d object detection from multi-view images via 3d-to-2d queries. In *Conference on Robot Learning*, 2022.
- [9] Xuanyao Chen, Tianyuan Zhang, Yue Wang, Yilun Wang, and Hang Zhao. Futr3d: A unified sensor fusion framework for 3d detection. *arXiv:2203.10642*, 2022.
- [10] Yingfei Liu, Tiancai Wang, Xiangyu Zhang, and Jian Sun. Petr: Position embedding transformation for multi-view 3d object detection. *arXiv:2203.05625*, 2022.
- [11] Xizhou Zhu, Weijie Su, Lewei Lu, Bin Li, Xiaogang Wang, and Jifeng Dai. Deformable detr: Deformable transformers for end-to-end object detection. *International Conference on Learning Representations*, 2021.
- [12] Wenwei Zhang, Zhe Wang, and Chen Change Loy. Exploring data augmentation for multi-modality 3d object detection. *arXiv:2012.12741*, 2020.
- [13] Charles R Qi, Li Yi, Hao Su, and Leonidas J Guibas. Pointnet++: Deep hierarchical feature learning on point sets in a metric space. In *Advances in Neural Information Processing Systems*, 2017.
- [14] Zetong Yang, Yanan Sun, Shu Liu, Xiaoyong Shen, and Jiaya Jia. Std: Sparse-to-dense 3d object detector for point cloud. In *IEEE/CVF International Conference on Computer Vision*, 2019.
- [15] Shaoshuai Shi, Xiaogang Wang, and Hongsheng Li. Pointrcnn: 3d object proposal generation and detection from point cloud. In *IEEE Conference on Computer Vision and Pattern Recognition*, 2019.
- [16] Charles R Qi, Or Litany, Kaiming He, and Leonidas J Guibas. Deep hough voting for 3d object detection in point clouds. In *IEEE/CVF International Conference on Computer Vision*, 2019.
- [17] Benjamin Graham and Laurens van der Maaten. Submanifold sparse convolutional networks. *arXiv:1706.01307*, 2017.
- [18] Yukang Chen, Yanwei Li, Xiangyu Zhang, Jian Sun, and Jiaya Jia. Focal sparse convolutional networks for 3d object detection. In *IEEE Conference on Computer Vision and Pattern Recognition*, 2022.
- [19] Bin Yang, Wenjie Luo, and Raquel Urtasun. Pixor: Real-time 3d object detection from point clouds. In *IEEE Conference on Computer Vision and Pattern Recognition*, 2018.
- [20] Bin Yang, Ming Liang, and Raquel Urtasun. Hdnet: Exploiting hd maps for 3d object detection. In *Conference on Robot Learning*, 2018.
- [21] Alex H Lang, Sourabh Vora, Holger Caesar, Lubing Zhou, Jiong Yang, and Oscar Beijbom. Pointpillars: Fast encoders for object detection from point clouds. In *IEEE Conference on Computer Vision and Pattern Recognition*, 2019.
- [22] Yan Yan, Yuxing Mao, and Bo Li. Second: Sparsely embedded convolutional detection. *Sensors*, 2018.
- [23] Jiajun Deng, Shaoshuai Shi, Peiwei Li, Wengang Zhou, Yanyong Zhang, and Houqiang Li. Voxel r-cnn: Towards high performance voxel-based 3d object detection. In *AAAI Conference on Artificial Intelligence*, 2021.
- [24] Tianwei Yin, Xingyi Zhou, and Philipp Krahenbuhl. Center-based 3d object detection and tracking. In *IEEE Conference on Computer Vision and Pattern Recognition*, 2021.

- [25] Garrick Brazil and Xiaoming Liu. M3d-rpn: Monocular 3d region proposal network for object detection. In *IEEE/CVF International Conference on Computer Vision*, 2019.
- [26] Andrea Simonelli, Samuel Rota Bulo, Lorenzo Porzi, Manuel López-Antequera, and Peter Kotschieder. Disentangling monocular 3d object detection. In *IEEE/CVF International Conference on Computer Vision*, 2019.
- [27] Tai Wang, Xinge Zhu, Jiangmiao Pang, and Dahua Lin. Fcos3d: Fully convolutional one-stage monocular 3d object detection. In *IEEE/CVF International Conference on Computer Vision*, 2021.
- [28] Rui Chen, Songfang Han, Jing Xu, and Hao Su. Point-based multi-view stereo network. In *IEEE/CVF International Conference on Computer Vision*, 2019.
- [29] Yilun Chen, Shu Liu, Xiaoyong Shen, and Jiaya Jia. Dsgn: Deep stereo geometry network for 3d object detection. In *IEEE Conference on Computer Vision and Pattern Recognition*, 2020.
- [30] Ming Liang, Bin Yang, Shenlong Wang, and Raquel Urtasun. Deep continuous fusion for multi-sensor 3d object detection. In *European Conference on Computer Vision*, 2018.
- [31] Tengteng Huang, Zhe Liu, Xiwu Chen, and Xiang Bai. Epnet: Enhancing point features with image semantics for 3d object detection. In *European Conference on Computer Vision*, 2020.
- [32] Tianwei Yin, Xingyi Zhou, and Philipp Krähenbühl. Multimodal virtual point 3d detection. *Advances in Neural Information Processing Systems*, 2021.
- [33] Xiaozhi Chen, Huimin Ma, Ji Wan, Bo Li, and Tian Xia. Multi-view 3d object detection network for autonomous driving. In *IEEE Conference on Computer Vision and Pattern Recognition*, 2017.
- [34] Jason Ku, Melissa Mozifian, Jungwook Lee, Ali Harakeh, and Steven L Waslander. Joint 3d proposal generation and object detection from view aggregation. In *IEEE/RSJ International Conference on Intelligent Robots and Systems*, 2018.
- [35] Jin Hyeok Yoo, Yecheol Kim, Jisong Kim, and Jun Won Choi. 3d-cvf: Generating joint camera and lidar features using cross-view spatial feature fusion for 3d object detection. In *European Conference on Computer Vision*, 2020.
- [36] Geoffrey Hinton, Oriol Vinyals, Jeff Dean, et al. Distilling the knowledge in a neural network. *arXiv:1503.02531*, 2015.
- [37] Xiaoyang Guo, Shaoshuai Shi, Xiaogang Wang, and Hongsheng Li. Liga-stereo: Learning lidar geometry aware representations for stereo-based 3d detector. In *IEEE/CVF International Conference on Computer Vision*, 2021.
- [38] Tsung-Yi Lin, Piotr Dollár, Ross Girshick, Kaiming He, Bharath Hariharan, and Serge Belongie. Feature pyramid networks for object detection. In *IEEE Conference on Computer Vision and Pattern Recognition*, 2017.
- [39] Jonah Philion and Sanja Fidler. Lift, splat, shoot: Encoding images from arbitrary camera rigs by implicitly unprojecting to 3d. In *European Conference on Computer Vision*, 2020.
- [40] Byeongho Heo, Jeesoo Kim, Sangdoo Yun, Hyojin Park, Nojun Kwak, and Jin Young Choi. A comprehensive overhaul of feature distillation. In *IEEE/CVF International Conference on Computer Vision*, 2019.
- [41] Nicolas Carion, Francisco Massa, Gabriel Synnaeve, Nicolas Usunier, Alexander Kirillov, and Sergey Zagoruyko. End-to-end object detection with transformers. In *European Conference on Computer Vision*, 2020.
- [42] Harold W Kuhn. The hungarian method for the assignment problem. *Naval research logistics quarterly*, 1955.
- [43] Holger Caesar, Varun Bankiti, Alex H Lang, Sourabh Vora, Venice Erin Liou, Qiang Xu, Anush Krishnan, Yu Pan, Giancarlo Baldan, and Oscar Beijbom. nuscenes: A multimodal dataset for autonomous driving. In *IEEE Conference on Computer Vision and Pattern Recognition*, 2020.
- [44] MMDetection3D Contributors. MMDetection3D: OpenMMLab next-generation platform for general 3D object detection. <https://github.com/open-mmlab/mmdetection3d>, 2020.
- [45] Zetong Yang, Yanan Sun, Shu Liu, and Jiaya Jia. 3dssd: Point-based 3d single stage object detector. In *IEEE Conference on Computer Vision and Pattern Recognition*, 2020.
- [46] Qi Chen, Lin Sun, Zhixin Wang, Kui Jia, and Alan Yuille. Object as hotspots: An anchor-free 3d object detection approach via firing of hotspots. In *European Conference on Computer Vision*, 2020.
- [47] Yihan Hu, Zhuangzhuang Ding, Runzhou Ge, Wenxin Shao, Li Huang, Kun Li, and Qiang Liu. Afdetv2: Rethinking the necessity of the second stage for object detection from point clouds. *AAAI Conference on Artificial Intelligence*, 2022.

- [48] Dennis Park, Rares Ambrus, Vitor Guizilini, Jie Li, and Adrien Gaidon. Is pseudo-lidar needed for monocular 3d object detection? In *IEEE/CVF International Conference on Computer Vision*, 2021.
- [49] Shaoqing Xu, Dingfu Zhou, Jin Fang, Junbo Yin, Zhou Bin, and Liangjun Zhang. Fusionpainting: Multimodal fusion with adaptive attention for 3d object detection. In *IEEE International Conference on Intelligent Transportation Systems*, 2021.
- [50] Chunwei Wang, Chao Ma, Ming Zhu, and Xiaokang Yang. Pointaugmenting: Cross-modal augmentation for 3d object detection. In *IEEE Conference on Computer Vision and Pattern Recognition*, 2021.

## A Experimental Details

In this section, we provide more technical details of the proposed UVTR. Because of the inherent properties, LiDAR- and camera-based methods usually adopt different pipelines for network training. For instance, GT-sampling and global augmentation are adopted for LiDAR-based approaches, while image-level augmentations are used for camera-based manners. To bridge the modality gap, we utilize the unified sampler and augmentation for network optimization.

**Unified Sampler.** Given point clouds of the captured scene, traditional LiDAR-based methods usually adopt GT-sampling [22] to supplement more samples from the whole database. However, due to the object overlapping in each view, this is seldom used for camera-based manners. In this work, we follow previous studies [50, 7] and use a unified approach for GT-sampling. In particular, we first generate point clouds and image crops of each sample from training scenes. For the multi-modality setting like UVTR-M in Tables 7 and 8, point clouds of sampled objects are attached to the original scene, and image crops are reorganized according to the actual depth and then pasted on the original image. For LiDAR-based settings, only point clouds are sampled for training, which is the same as previous work. The unified sampler is disabled at the last 2 epochs to fit the normal distribution.

**Unified Augmentation.** With the unified representation, global augmentations can be synchronized in the voxel space. Specifically, given the widely-adopted global scaling, rotation, and flipping for point clouds, we apply the same augmentations to the image voxel space  $\mathbf{V}_I$ . That means we first construct the voxel space  $\mathbf{V}_I$  for images and then conduct space-level augmentations to stay the same with that of point cloud  $\mathbf{V}_P$ . In this manner, both modalities are well aligned in augmentation for cross-modality interactions and the following object-level interaction in the transformer decoder. For LiDAR-based and multi-modality settings, we adopt all the augmentations during training. For camera-based settings, only global scaling and rotation are applied to image voxel space  $\mathbf{V}_I$ .

**Training Schedule.** In Section 4.1 of the main paper, we give training details with different modalities. To be more specific, for the multi-modality setting, we finetune the framework for 20 epochs, which may not be fully optimized. Following previous work [50, 7], CBGS sampler is utilized for class balance optimization in the training process. Specifically, we initialize the camera- or LiDAR-based branch from the corresponding pretrained model and reduce the total training epoch to 10. In Table 9, we compare with previous methods on the nuScenes dataset. Obviously, the proposed UVTR can further be improved to 70.6% NDS and 65.9% mAP with CBGS on the nuScenes *val* set.

Table 9: Comparisons among different methods with a single model on the nuScenes *val* set. We compare with classic methods on the multi-modality setting. M indicates the Multi-modality input.

Method	Backbone	NDS(%)	mAP(%)	mATE $\downarrow$	mASE $\downarrow$	mAOE $\downarrow$	mAVE $\downarrow$	mAAE $\downarrow$
<i>LiDAR+Camera</i>								
FUTR3D [9]	V0.075-R101	68.3	64.5	-	-	-	-	-
UVTR-M	V0.075-R101	70.2	65.4	0.332	0.258	0.268	0.212	0.177
UVTR-M-CBGS	V0.075-R101	<b>70.6</b>	<b>65.9</b>	0.320	0.256	0.262	0.219	0.176

**Training Setting.** Due to different pipelines, we construct each training batch on 8 devices with 32, 8, and 16 input data for LiDAR-, camera-based, and multi-modality settings, respectively. For camera-based setting, we initialize our image backbone from the pretrained FCOS3D [27]. Most of our models are trained on NVIDIA V100 GPU. Part of memory-consuming models with multi-frame or multi-modality settings like UVTR-CS and UVTR-M are trained on NVIDIA A100 GPU.

**Inference Setting.** In the inference stage, we keep 300 top-scoring predictions within the range  $[-10m, -10m]$  for  $Z$  axis and  $[-61.2m, -61.2m]$  for  $X$  and  $Y$  axis.

## B Qualitative Analysis

In this section, we give visualizations of UVTR predictions on different modalities and different views, as presented in Figures 6 and 7. We draw the predicted results on LiDAR-based BEV views and each camera view for clear comparisons. It is clear that UVTR performs well on nuScenes [43] dataset, and most of the objects are detected in these scenes.

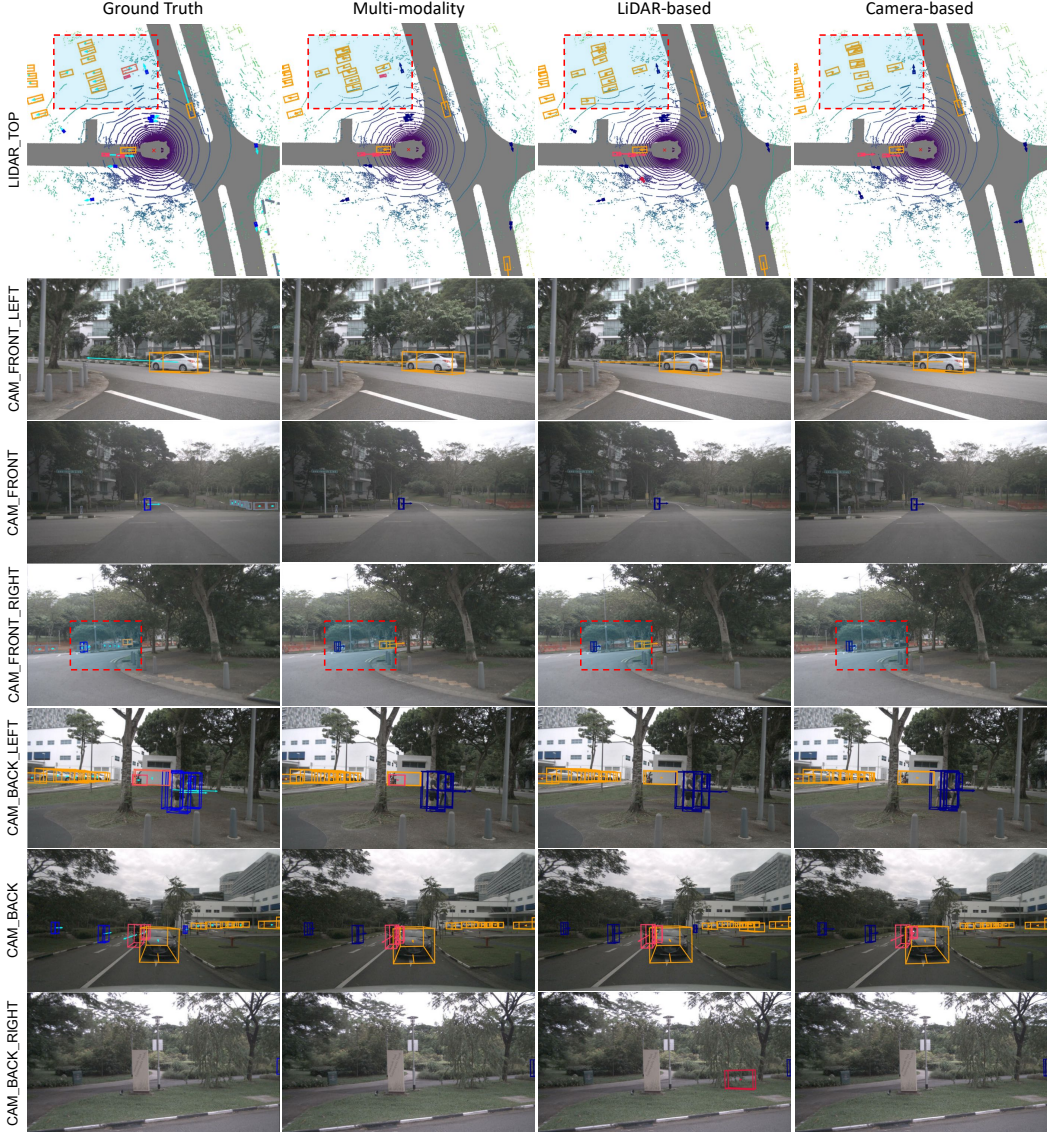


Figure 6: Visualization of UVTR predictions with different modalities on nuScenes *val* set. The important area that needs more attention is marked with dotted red box. Best viewed in color.

**Multi-modality Results.** The multi-modality results are given in the second column of Figures 6 and 7. Compared with the ground truth, the multi-modality detector gives accurate predictions of object location, category, speed, and orientation (arrows in each figure). Although the multi-modality setting introduces advantages from both LiDAR and camera, there still exists missing objects, especially for far or small objects. It remains potential to be further explored for these cases.

**LiDAR-based Results.** For LiDAR-based detector, predictions are presented in the third column of Figures 6 and 7. Different from that of multi-modality results, the LiDAR-based method lacks sufficient context from images for accurate classification and thus brings the wrong detection. For example, without surrounding context, the *tree* in last row of Figure 6 is detected as *vehicle*.

**Camera-based Results.** For camera-based approach, we plot results in the last column of Figures 6 and 7. Because accurate positions are missing in images, locations of predicted boxes are not so accurate. But the camera-based manner provides more context cues for better recognition. As shown in the second row of Figure 7, *barriers* are well detected with the aid of images for camera-based and multi-modality methods, while this is not the case for LiDAR-based manner.

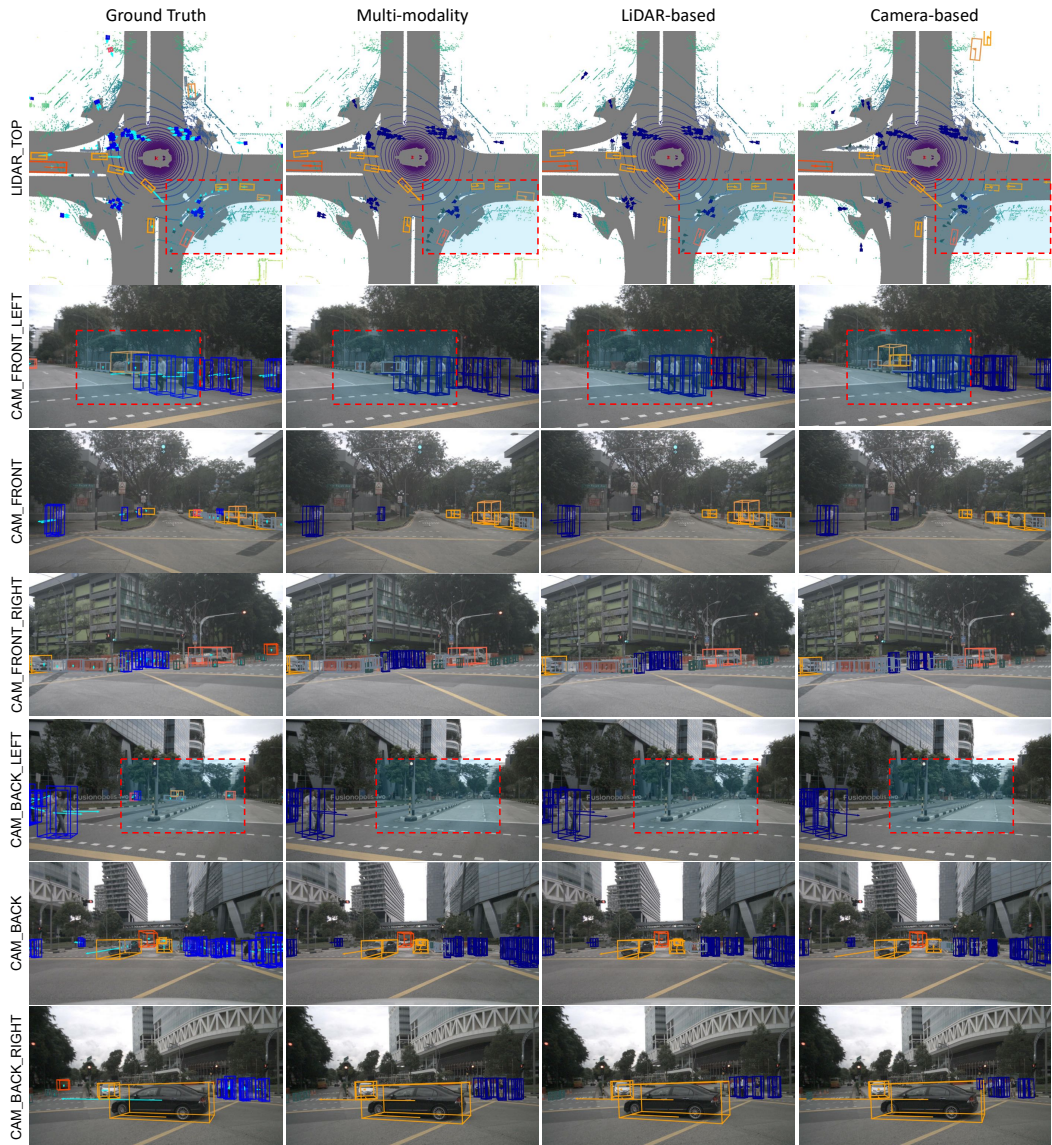


Figure 7: Extended visualization of UVTR predictions with different modalities on nuScenes val set. The important area that needs more attention is marked with dotted red box. Best viewed in color.